Combustion and Flame 157 (2010) 1850–1862

Contents lists available at ScienceDirect

Combustion and Flame

journal homepage: www.elsevier.com/locate/combustflame

Prediction of autoignition in a lifted methane/air flame using an unsteady flamelet/progress variable model

Matthias Ihme *, Yee Chee See

Department of Aerospace Engineering, University of Michigan, Ann Arbor, MI 48109, United States

ARTICLE INFO

Article history:
Received 19 July 2009
Received in revised form 27 September 2009
Accepted 15 July 2010
Available online 3 August 2010

Keywords:
Turbulent combustion
Autoignition
Lifted flames
Non-premixed combustion
Unsteady flamelet modeling
Large-eddy simulation

ABSTRACT

An unsteady flamelet/progress variable (UFPV) model has been developed for the prediction of autoignition in turbulent lifted flames. The model is a consistent extension to the steady flamelet/progress variable (SFPV) approach, and employs an unsteady flamelet formulation to describe the transient evolution of all thermochemical quantities during the flame ignition process. In this UFPV model, all thermochemical quantities are parameterized by mixture fraction, reaction progress parameter, and stoichiometric scalar dissipation rate, eliminating the explicit dependence on a flamelet time scale. An *a priori* study is performed to analyze critical modeling assumptions that are associated with the population of the flamelet state space.

For application to LES, the UFPV model is combined with a presumed PDF closure to account for subgrid contributions of mixture fraction and reaction progress variable. The model was applied in LES of a lifted methane/air flame. Additional calculations were performed to quantify the interaction between turbulence and chemistry *a posteriori*. Simulation results obtained from these calculations are compared with experimental data. Compared to the SFPV results, the unsteady flamelet/progress variable model captures the autoignition process, and good agreement with measurements is obtained for mixture fraction, temperature, and species mass fractions. From the analysis of scatter data and mixture fraction-conditional results it is shown that the turbulence/chemistry interaction delays the ignition process towards lower values of scalar dissipation rate, and a significantly larger region in the flamelet state space is occupied during the ignition process.

© 2010 The Combustion Institute. Published by Elsevier Inc. All rights reserved.

1. Introduction

The development of advanced combustion systems is mainly controlled by the objective to increase fuel efficiency and to reduce emissions of pollutants such as carbon monoxide (CO), unburned hydrocarbons (UHC), and nitrogen oxides (NO_x). To address these issues, combustion strategies have been developed that utilize combustion of lean and diluted fuel–air mixtures. In these systems, dilution is frequently accomplished through the recirculation of burned gases, which reduces the combustion temperature, and inhibits the formation of thermal nitric oxide. In addition to reduced pollutant emissions, the dilution with hot combustion products can also lead to improved flame stability [1].

Despite its enormous potential, the stable combustion of lean and diluted fuel–air mixtures introduces considerable challenges. In particular, the dilution of reactants with inert combustion products can lead to a reduction in the characteristic Damköhler number, so that – unlike conventional diffusion flames, in which the combustion process is primarily mixing-controlled – the reaction kinetics becomes increasingly important. As such, the stability and characteristics of the flame becomes particularly sensitive to variations in fuel composition and operating conditions. Therefore, ignition mechanisms in such flames play a critical role and are directly affected by the turbulence/chemistry interaction.

Recently, Yoo et al. [2] performed direct numerical simulations (DNS) to investigate autoignition of a lifted hydrogen flame in a coflow at elevated temperature. Their results showed that the flame stabilizes in regions where the reactants are incompletely mixed and autoignition occurs under conditions in which gradients of fuel and oxidizer are oriented in opposite directions. The autoignition process could be associated with the accumulation of hydroperoxyl (HO_2) upstream of the flamebase, providing a source of hydroxyl (OH) radicals for the autoignition. With increasing downstream distance, the heat release extends towards the fuel-rich composition and occurs under premixed and non-premixed conditions.

Autoignition of a fuel mixture in a hot environment is typically initiated in localized regions of low scalar dissipation rates having a mixture composition that favors short ignition times. Since the prediction of autoignition events is strongly dependent on the structure of the surrounding turbulent reacting flow environment, combustion models are required that are able to provide an

* Corresponding author. Fax: +1 734 763 0578.
E-mail address: mihme@umich.edu (M. Ihme).

0010-2180/$ - see front matter © 2010 The Combustion Institute. Published by Elsevier Inc. All rights reserved.
doi:10.1016/j.combustflame.2010.07.015

accurate characterization of the spatiotemporal flow field structure. Although large-eddy simulation (LES) techniques have been demonstrated to provide improved predictions for the turbulent mixing process compared to Reynolds-averaged Navier–Stokes (RANS) approaches [3], these intermittent ignition events typically occur on scales that are computationally not resolved. Therefore, subgrid-scale closure models are required to characterize effects of unresolved scales and ignition kinetics. By addressing these issues, the objective of this work is to develop a LES combustion model for application to autoignition in turbulent non-premixed flames. To this end, an unsteady flamelet formulation that was developed by Pitsch and Ihme [4] is extended. In this model, the transient flame evolution is characterized by mixture fraction, reaction progress variable, and scalar dissipation rate, and the flame structure is obtained from the unsteady flamelet equations. A potential advantage over related formulations [5] is that this model eliminates the explicit dependence on the time-scale information which leads to significant simplifications in the computation and parameterization of the thermodynamic state space.

The LES autoignition model is applied to a lifted methane/air jet flame. This flame configuration was experimentally investigated by Cabra et al. [6], and consists of a central fuel jet which issues a methane/air mixture into a vitiated co-flow. The temperature of the co-flow stream is 1355 K. Following a region in which fuel and oxidizer mix without significant heat release, the flame ignites and stabilizes at a lift-off height of approximately 30 nozzle diameters downstream of the jet exit.

Because of its canonical geometry, comprehensive experimental database, and sensitivity of the flame characteristics to operating conditions, this flame configuration has gained particular interest in the computational combustion community, and is frequently used for validation and development of combustion models. Gordon et al. [7] investigated the transport budget of this flame using a composition PDF approach. From this study they concluded that the flame stabilization mechanism is primarily controlled by autoignition. A joint scalar transported PDF approach with detailed reaction chemistry coupled with a second moment closure model for the velocity prediction was used by Gkagkas and Lindstedt [8] to compute this lifted flame. Their model reproduced the flow field sensitivity to boundary conditions, and the role of hydroperoxyl and formaldehyde on the ignition kinetics was characterized. Domingo et al. [9] performed a LES calculation of this flame. They combined a model for autoignition in a perfectly stirred reactor (PSR) with a model for partially premixed flame propagation, and good agreement between simulation results and experimental data was obtained. More recently, Michel et al. [10] conducted a RANS simulation of this flame using an approximate diffusion flame approach. In this approach, the transient flame states are obtained from a PSR calculation, and diffusive effects are considered *a posteriori* through the solution of a diffusion flamelet equation for a progress variable.

In this context it is interesting to point out that all of these calculations employed combustion models that either rely on a transported PDF approach or a formulation in which a PSR model is employed to model the autoignition process. However, non-premixed combustion models have so far not been applied to this flame. This paper addresses this shortcoming, and specifically focuses on two aspects, namely the characterization of transient effects in the context of diffusion flames, and the role of the turbulence/chemistry interaction that is of particular relevance to LES applications.

The remainder of this paper is organized as follows. The mathematical model describing the unsteady flamelet/progress variable formulation and the presumed PDF closure is presented in the next section. The experimental configuration and computational setup are summarized in Section 3. An *a priori* study is performed in Section 4 to analyze critical modeling assumptions that are associated with the population of the flamelet state space. Following this *a priori* study, the model is applied in LES, and simulation results are discussed in Section 5. The paper finishes with conclusions.

2. Mathematical model

2.1. Large-eddy simulation

In LES, coherent large scale structures of the turbulent flow are computationally resolved, and effects of smaller and numerically unresolved scales on the large scales are modeled. The decomposition of the scales is achieved by applying a low-pass filter to the flow field quantities. In the case of a reacting flow, the Favre-filtered quantity of a scalar ψ is computed as

$$\widetilde{\psi}(t,\boldsymbol{x}) = \frac{1}{\overline{\rho}} \int \rho(t,\boldsymbol{y})\psi(t,\boldsymbol{y})G(t,\boldsymbol{x},\boldsymbol{y};\Delta)d\boldsymbol{y}, \tag{1}$$

where t denotes time, $\boldsymbol{x}$ is the spatial coordinate, ρ is the density, and G is the filter kernel. The residual field is defined as $\psi''(t,\boldsymbol{x}) = \psi(t,\boldsymbol{x}) - \widetilde{\psi}(t,\boldsymbol{x})$ and Favre-filtered quantities are related to Reynolds-filtered quantities by $\overline{\rho}\widetilde{\psi} = \overline{\rho\psi}$.

After applying the filter operator to the instantaneous governing equations, describing the conservation of mass and momentum, the Favre-filtered equations can be written as

$$\widetilde{\mathscr{D}}_t\overline{\rho} = -\overline{\rho}\nabla\cdot\widetilde{\boldsymbol{u}}, \tag{2a}$$

$$\overline{\rho}\widetilde{\mathscr{D}}_t\widetilde{\boldsymbol{u}} = -\nabla\overline{p} + \nabla\cdot\underline{\underline{\overline{\sigma}}} + \nabla\cdot\underline{\underline{\sigma}}^{\mathrm{res}}, \tag{2b}$$

where $\overline{\rho}$ is the filtered density, $\widetilde{\mathbf{u}}$ is the filtered velocity vector, $\overline{p}$ is the filtered pressure, $\widetilde{\mathscr{D}}_t = \partial_t + \widetilde{\boldsymbol{u}}\cdot\nabla$ is the Favre-filtered substantial derivative, and $\underline{\underline{\overline{\sigma}}}$ is the filtered viscous stress tensor with

$$\underline{\underline{\overline{\sigma}}} = 2\overline{\rho}\overline{\nu}\left[\underline{\underline{\widetilde{S}}} - \frac{1}{3}(\nabla\cdot\widetilde{\mathbf{u}})\underline{\underline{I}}\right] \quad \text{and} \quad \underline{\underline{\widetilde{S}}} = \frac{1}{2}[\nabla\widetilde{\boldsymbol{u}} + (\nabla\widetilde{\boldsymbol{u}})^T]. \tag{3}$$

The residual stress tensor, $\underline{\underline{\sigma}}^{\mathrm{res}} = \overline{\rho}\widetilde{\boldsymbol{u}}\widetilde{\boldsymbol{u}} - \overline{\rho}\widetilde{\boldsymbol{u}\boldsymbol{u}}$, appears in unclosed form, and is modeled by a dynamic Smagorinsky model [11,12]. In deriving Eq. (2) a time-invariant filter is used, and commutation errors due to grid size variations are neglected [13]. The density and molecular properties, appearing in Eqs. (2) and (3), and all other thermochemical quantities are obtained from the flamelet/progress variable model. This model and its extension to autoignition prediction are discussed in the next sections.

2.2. Flamelet/progress variable model

The flamelet/progress variable (FPV) model [14,15] is based on the flamelet equations, in which a turbulent diffusion flame is represented as an ensemble of laminar flame structures [16,17]. For sufficiently large Damköhler number or activation energy, chemical reactions and heat transfer occur in a thin layer. If the characteristic length scale of this layer is small compared to that of the surrounding turbulence, turbulent structures are unable to penetrate into the reaction zone and cannot destroy the flame structure. Therefore, effects of turbulence only result in a deformation and straining of the flame sheet.

The flamelet equations are obtained through a coordinate transformation of the transport equations for species mass fraction and temperature [16,17], in which the mixture fraction Z is introduced as an independent variable. The unsteady flamelet equations can then be written as

$$\partial_t\boldsymbol{\phi} - \frac{\chi_Z}{2}\partial_Z^2\boldsymbol{\phi} = \dot{\boldsymbol{\omega}}, \tag{4}$$

where $\dot{\boldsymbol{\omega}}$ corresponds to the source term of all species and temperature, which are collectively denoted by the vector $\boldsymbol{\phi}$. The scalar dissipation rate of the mixture fraction, appearing in Eq. (4), is

$$\chi_Z = 2\alpha|\nabla Z|^2, \tag{5}$$

and α is the mass diffusivity, which is assumed to be equal for all species. An analytical expression for χ_Z for a counter-flow diffusion flame was derived by Peters [18]. This expression relates χ_Z to its value at stoichiometric condition and is a function of Z and Z_{st}:

$$\chi_Z = \chi_{Z,st} F(Z)$$

with

$$F(Z) = \exp\left\{2\left(\left[\text{erfc}^{-1}(2Z_{st})\right]^2 - [\,\text{erfc}^{-1}(2Z)]^2\right)\right\}, \tag{6}$$

and erfc^{-1} denotes the inverse of the complementary error function.

2.3. Steady flamelet/progress variable (SFPV) model

The steady flamelet equations can be derived from Eq. (4) under the consideration that all species are formed on a sufficiently fast time scale, so that all species mass fractions and temperature are in quasi steady state. With this, temporal derivatives become negligible, and Eq. (4) reduces to

$$-\frac{\chi_Z}{2}\partial_Z^2\boldsymbol{\phi} = \dot{\boldsymbol{\omega}}. \tag{7}$$

The solution of these equations can be represented by the so-called S-shaped curve [18], and all thermochemical quantities can then be parameterized in terms of mixture fraction and scalar dissipation rate, *viz.*,

$$\boldsymbol{\psi} = \mathscr{E}_{\boldsymbol{\psi}}(Z, \chi_{Z,st}), \tag{8}$$

in which $\mathscr{E}_{\boldsymbol{\psi}}$ corresponds to the steady-state flamelet relation, and $\boldsymbol{\psi}$ denotes all thermochemical quantities, including molecular properties, density, temperature, species mass fractions, and chemical source terms. The Favre-filtered form of this state relation can be used to provide information about density and molecular properties that are necessary to solve Eq. (2). In addition to the governing equations describing conservation of mass and momentum, an additional transport equation for the mixture fraction must be solved, and the scalar dissipation rate can be obtained from an algebraic relation. Note however, that this representation is not unique and results in multiple solutions for certain values of scalar dissipation rates.

To overcome the ambiguity of the steady flamelet model, a reaction progress parameter Λ has been introduced in the SFPV model [15]. This mixture fraction-independent parameter, which is related to the reaction progress variable C, is defined so that each flamelet along the entire S-shaped curve can be uniquely identified. In the following, the reaction progress variable is defined from a linear combination of reaction products as $C = Y_{CO} + Y_{CO_2} + Y_{H_2O} + Y_{H_2}$. If for each flamelet Λ is associated with the corresponding C at stoichiometric condition, a unique mapping between $\chi_{Z,st}$ and Λ along the entire S-shaped curve is obtained. Figure 1 illustrates this mapping procedure. The top panel shows the temperature and the reaction progress variable as a function of $\chi_{Z,st}$. The bottom panel shows the corresponding data for T_{st}, obtained by remapping the solution from $\chi_{Z,st}$ onto the reaction progress parameter Λ. The results illustrated in this figure emphasize the unique representation of each flamelet along the entire S-shaped curve. By remapping Eq. (8), the SFPV state relation can be written as

$$\boldsymbol{\psi} = \mathscr{F}^{S}_{\boldsymbol{\psi}}(Z, \Lambda), \tag{9}$$

where the superscript "S" refers to the steady flamelet equations in the SFPV model. This relation is used instead of Eq. (8) to represent the complete thermochemical state space along the entire S-shaped curve.

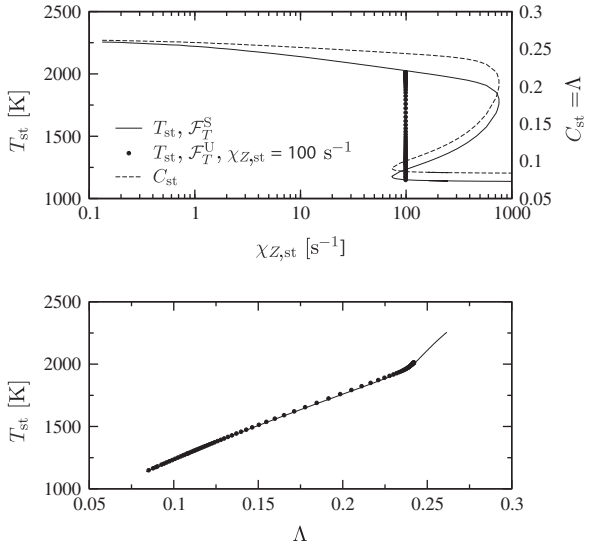

Fig. 1. Mapping between C and Λ: The top panel shows the temperature and reaction progress variable as a function of $\chi_{Z,st}$ along the entire S-shaped curve. By remapping the same data onto the reaction progress parameter Λ (shown in the bottom panel) a unique representation of the entire S-shaped curve is obtained. For reference, an unsteady flamelet trajectory for a constant scalar dissipation rate of $\chi_{Z,st} = 100$ s^{-1} is shown by the symbols.

Although this SFPV model has been successfully applied to a wide range of combustion configurations, due to the neglect of the transient term in the steady flamelet equations, this model is inadequate for the prediction of autoignition events. To overcome this limitation, an unsteady flamelet/progress variable (UFPV) model is developed in the next section. This model extends the work of Pitsch and Ihme [4] by employing a statistically most-likely PDF to model subgrid scale fluctuations of the reaction progress variable. After presenting the UFPV model in the next section, the presumed PDF closure model is discussed in Section 2.5.

2.4. Unsteady flamelet/progress variable (UFPV) model for autoignition

Models employing the steady flamelet formulation restrict the flamelet solution to that of the S-shaped curve. In fact, models in which all thermochemical quantities are parameterized in the form of Eq. (8) can only use a subset of the steady flamelet solution space due to the non-uniqueness of the parameterization. Although the S-shaped curve represents the strong attractor of the flamelet equations in the limit of sufficiently long residence time, for the consideration of transient and autoignition events, the complete state space must be considered, requiring the solution of the unsteady flamelet equations.

Unsteady flamelet models have been used in LES applications [5]. In addition to the local scalar dissipation rate and mixture fraction, these formulations rely on a local flamelet time that is associated with the convection and diffusion of each flamelet. As such, the required information about the state-space trajectory and the corresponding time for each flamelet limits their application to canonical flows. The unsteady flamelet/progress variable model addresses this limitation by expressing the flamelet time in terms of reaction progress parameter and scalar dissipation rate. All thermochemical quantities, obtained from the solution of the unsteady flamelet Eq. (4), are then parameterized in the form of

$$\boldsymbol{\psi} = \mathscr{F}^{U}_{\boldsymbol{\psi}}(Z, \Lambda, \chi_{Z,st}), \tag{10}$$

where the superscript "U" refers to the unsteady flamelet library. With this relation, differential changes of a state-space variable $\boldsymbol{\psi}$ are then represented by

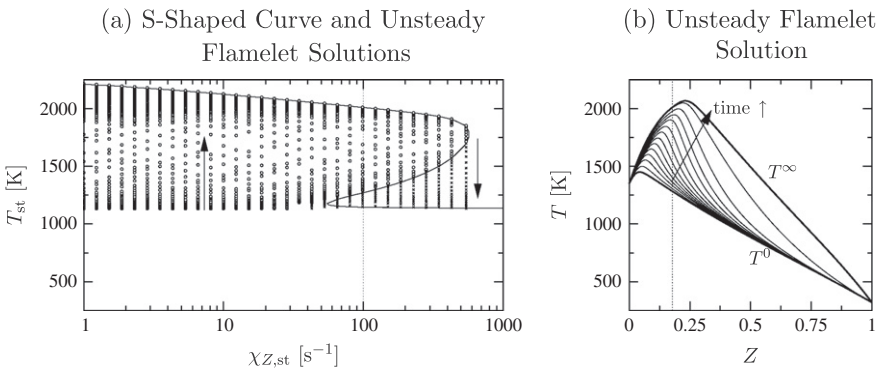

Fig. 2. Solutions of the flamelet equations for a methane/air flame, showing (a) temperature as function of the scalar dissipation rate at stoichiometric mixture fraction $Z_{st} = 0.177$; the symbols correspond to solutions of the unsteady flamelet equations, and the solid line represents the S-shaped curve, obtained from the steady flamelet equations. The directions for igniting and extinguishing flamelets are identified by arrows. (b) Temperature profiles, showing the evolution of a flamelet with increasing time, computed for a scalar dissipation rate of $\chi_{Z,st} = 100\ s^{-1}$, and the vertical dashed line shows the location of the stoichiometric mixture fraction.

$$d\psi = \frac{\partial \psi}{\partial Z} dZ + \frac{\partial \psi}{\partial \Lambda} d\Lambda + \frac{\partial \psi}{\partial \chi_{Z,st}} d\chi_{Z,st}. \tag{11}$$

Since this expression eliminates the time from the parameterization, it also assumes that the structure of a particular flamelet is independent of its history. This in turn allows the population of the state space independently from a particular flamelet trajectory. In the context of the prediction of radiation and NO pollutant formation, it was shown that the flamelet history is typically not important for species evolving on sufficiently fast time scales [19]. However, the DNS by Yoo et al. [2] showed that the autoignition of a hydrogen flame is preceded by the formation of stable HO_2 species upstream of the flamebase, suggesting that the flamelet trajectory could become relevant at the ignition location. In order to assess the significance of the flamelet history in the UFPV model, an *a priori* study of the model will be performed in Section 4.

In the UFPV model, the unsteady state-space is populated as follows. First, the S-shaped curve is obtained from the solution of the steady flamelet equations. To obtain solutions 'inside' the S-shaped curve, starting with the initial conditions corresponding to the middle branch or a non-burning flamelet, the unsteady flamelet equations are solved for a specified scalar dissipation rate until the stable solution of the upper branch is reached. If the steady-state solution is reached, the process is repeated with a different value for the scalar dissipation until the complete state space is populated. In this respect, the flamelet trajectory corresponds to a vertical line in the state space. Figure 2a illustrates the result of this procedure. The symbols correspond to individual solutions of the unsteady flamelet equations. The solutions are obtained from the previously described method, and the solid line is the S-shaped curve from the steady flamelet equations.

Figure 2b shows the temporal evolution of a flamelet for a constant scalar dissipation rate of $\chi_{Z,st} = 100\ s^{-1}$. Beginning with a flamelet from the unstable middle branch, the flamelet ignites at a location at fuel-lean conditions, corresponding to the most-reactive mixture [20]. By diffusive transport in mixture fraction space, the flame structure evolves over about 2.5 ms until the steady-state condition is reached. This steady-state solution is denoted by the superscript "∞."

The ignition delay time τ_{ig} as function of $\chi_{Z,st}$ is shown in Fig. 3. Here, τ_{ig} is evaluated at stoichiometric condition, and is defined as:

$$\tau_{ig} = \left\{ t \middle| T_{st}(t) = \left(T^0_{st} + T^\infty_{st} \right) \middle/ 2 \right\}, \tag{12}$$

where T^0 and T^∞ denote the temperature profiles of the non-burning and steady burning flamelet solution, respectively. Beginning at the location corresponding to $\chi_{Z,i}$, which corresponds to the critical scalar dissipation rate below which an initially non-burning flamelet will ignite, the ignition delay time decreases until it reaches a minimum of $\tau_{ig} = 2.95$ ms at $\chi_{Z,st} = 14.5\ s^{-1}$, and subsequently increases with decreasing scalar dissipation rate. For comparison, a PSR calculation with a mixture corresponding to the stoichiometric condition of a non-reacting diffusion flamelet has been performed. From this homogeneous autoignition simulation an ignition delay time of $\tau_{ig} = 170$ ms was obtained which is more than 50 times slower compared to the minimum ignition time shown in Fig. 3.

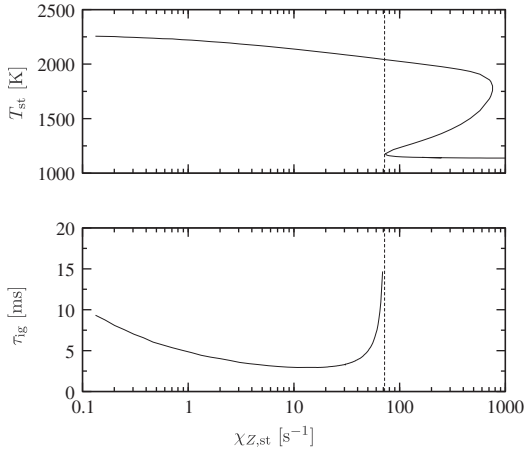

Fig. 3. Ignition delay time as function of $\chi_{Z,st}$.

In Section 4, an *a priori* study of the UFPV model is performed to quantify the significance of transient effects. This study allows us to assess critical assumptions that have been invoked in the development of the UFPV model, and to identify differences to the SFPV model.

In turbulent reacting flows, the flame structure is affected by the turbulent environment, which requires the consideration of turbulence/chemistry interaction. However, since the spatiotemporal structure of the flame is not fully resolved in LES, a statistical description of the flame structure is employed in this work. For this, a presumed PDF closure is used which is described in the next section.

2.5. Presumed PDF closure model

For the LES prediction of turbulent reacting flows, the state relation (10) must be formulated for Favre-filtered quantities. These quantities are computed by employing a presumed joint PDF for

mixture fraction, reaction progress parameter, and stoichiometric scalar dissipation rate:

$$\widetilde{\psi} = \int\int\int \mathscr{F}_{\psi}^{\mathrm{U}}(Z,\Lambda,\chi_{Z,\mathrm{st}})\widetilde{P}(Z,\Lambda,\chi_{Z,\mathrm{st}})dZ\,d\Lambda\,d\chi_{Z,\mathrm{st}}, \tag{13}$$

where $\widetilde{P}(Z,\Lambda,\chi_{Z,\mathrm{st}})$ denotes the density-weighted joint PDF with

$$\widetilde{P}(Z,\Lambda,\chi_{Z,\mathrm{st}}) = \frac{\rho}{\overline{\rho}}P(Z,\Lambda,\chi_{Z,\mathrm{st}}) = \widetilde{P}(Z,\chi_{Z,\mathrm{st}})P(\Lambda|Z,\chi_{Z,\mathrm{st}}). \tag{14}$$

Since Λ is defined to be statistically independent from Z and $\chi_{Z,\mathrm{st}}$, the conditional PDF $P(\Lambda|Z,\chi_{Z,\mathrm{st}})$ reduces to its marginal PDF. Furthermore, it is assumed that Z and $\chi_{Z,\mathrm{st}}$ are independent. With this, Eq. (14) can be written as

$$\widetilde{P}(Z,\Lambda,\chi_{Z,\mathrm{st}}) = \widetilde{P}(Z)P(\Lambda)P(\chi_{Z,\mathrm{st}}). \tag{15}$$

A beta PDF is used to model the mixture fraction distribution [21,22], and the distribution of $\chi_{Z,\mathrm{st}}$ is described by a delta function [4]. A statistically most-likely distribution (SMLD) [23–26] is employed for Λ, so that $\widetilde{P}(Z,\Lambda,\chi_{Z,\mathrm{st}})$ can be written as

$$\widetilde{P}(Z,\Lambda,\chi_{Z,\mathrm{st}}) = \beta(Z;\widetilde{Z},\widetilde{Z''^2})P_{\mathrm{SML},2}(\Lambda)\delta(\widetilde{\chi}_{Z,\mathrm{st}} - \chi_{Z,\mathrm{st}}), \tag{16}$$

with

$$P_{\mathrm{SML},j}(\Lambda) = \mathrm{Q}(\Lambda)\exp\left\{\sum_{i=0}^{j} a_i\Lambda^i\right\}, \tag{17}$$

where j(=2) denotes the number of enforced moments. To account for bias in composition space, the *a priori* PDF $Q(\Lambda)$ is introduced [27], which is modeled as [28]

$$Q(\Lambda) = \frac{1}{\sqrt{\widetilde{C''^2}}}\left[1 + \left(\frac{\dot{\omega}_{C,\mathrm{st}}\gamma_C\widetilde{Z''^2}}{\chi_{Z,\mathrm{st}}\sqrt{\widetilde{C''^2}}}\right)^2\right]^{1/2}. \tag{18}$$

This *a priori* PDF is a measure of the drift induced by chemical reaction and mixing of the progress variable at stoichiometric condition, and γ_C is the mixing frequency ratio between conserved and reactive scalar [18].

The unknown coefficients a_i in Eq. (17) are determined by constraining the moments of the reaction progress variable [28], and the joint PDF $\widetilde{P}(Z,\Lambda,\chi_{Z,\mathrm{st}})$ can be constructed from Eqs. (16) and (17) to obtain the Favre-filtered form of the thermochemical state relation. In this context it is interesting to point out that the joint PDF is not directly dependent on the moment information about the reaction progress parameter Λ. Therefore, all Favre-filtered thermochemical quantities can directly be expressed in terms of $\widetilde{C}$ and $\widetilde{C''^2}$. This relation is denoted by

$$\widetilde{\psi} = \widetilde{\mathscr{G}}_{\psi}^{\mathrm{U}}(\widetilde{Z},\widetilde{Z''^2},\widetilde{C},\widetilde{C''^2},\widetilde{\chi}_{Z,\mathrm{st}}). \tag{19}$$

Note that this relation introduces significant modeling simplifications, since it eliminated the explicit Λ-dependence. In the following, Eq. (19) is used to provide information about all thermochemical quantities in the conservation equations for mass and momentum. In addition to the solution of Eq. (2), four transport equations are required to close the system of equations in the UFPV model. The transport equations describing conservation of the first two moments of mixture fraction and progress variable can be written as

$$\overline{\rho}\widetilde{\mathscr{D}}_t\widetilde{Z} = \nabla\cdot(\overline{\rho}\widetilde{\alpha}\nabla\widetilde{Z}) + \nabla\cdot\boldsymbol{\tau}_{Z}^{\mathrm{res}}, \tag{20a}$$

$$\overline{\rho}\widetilde{\mathscr{D}}_t\widetilde{Z''^2} = \nabla\cdot(\overline{\rho}\widetilde{\alpha}\nabla\widetilde{Z''^2}) + \nabla\cdot\boldsymbol{\tau}_{\widetilde{Z''^2}}^{\mathrm{res}} - 2\overline{\rho}\widetilde{\boldsymbol{u}''Z''}\cdot\nabla\widetilde{Z} - \overline{\rho}\widetilde{\chi}_{Z}^{\mathrm{res}}, \tag{20b}$$

$$\overline{\rho}\widetilde{\mathscr{D}}_t\widetilde{C} = \nabla\cdot(\overline{\rho}\widetilde{\alpha}\nabla\widetilde{C}) + \nabla\cdot\boldsymbol{\tau}_{C}^{\mathrm{res}} + \overline{\rho}\widetilde{\dot{\omega}}_C, \tag{20c}$$

$$\overline{\rho}\widetilde{\mathscr{D}}_t\widetilde{C''^2} = \nabla\cdot(\overline{\rho}\widetilde{\alpha}\nabla\widetilde{C''^2}) + \nabla\cdot\boldsymbol{\tau}_{\widetilde{C''^2}}^{\mathrm{res}} - 2\overline{\rho}\widetilde{\boldsymbol{u}''C''}\cdot\nabla\widetilde{C} - \overline{\rho}\widetilde{\chi}_{C}^{\mathrm{res}} + 2\overline{\rho}\widetilde{C''\dot{\omega}_C''}. \tag{20d}$$

The turbulent fluxes $\widetilde{\boldsymbol{u}''Z''}$ and $\widetilde{\boldsymbol{u}''C''}$ are modeled by a gradient transport assumption [29], and the term $\widetilde{C''\dot{\omega}_C''}$ is precomputed and stored in the flamelet library. A model for the residual scalar dissipation rate of the mixture fraction is derived from spectral arguments [28], and can be written in the form

$$\widetilde{\chi}_{Z}^{\mathrm{res}} = \frac{C_{\chi_z}C_\epsilon}{C_u}\frac{\nu_t}{\Delta^2}\widetilde{Z''^2}. \tag{21}$$

The coefficient C_{χ_z} can be estimated using model energy spectra for turbulent kinetic energy and mixture fraction variance [30]. Based on this analysis, a value of 2.0 was used for this coefficient. The ratio C_ϵ/C_u is dependent on the LES filter width Δ, and rapidly approaches zero for increasing filter ratio Δ/η, with η denoting the Kolmogorov length scale [31]. For the present application, a value of 2.0 was used for the ratio C_ϵ/C_u.

A closure model for $\widetilde{\chi}_{C}^{\mathrm{res}}$ is developed from the mixing time scale ratio, which can be written as [18]:

$$\gamma_C = \frac{\tau_C}{\tau_Z} = \frac{\widetilde{C''^2}/\widetilde{\chi}_{C}^{\mathrm{res}}}{\widetilde{Z''^2}/\widetilde{\chi}_{Z}^{\mathrm{res}}}, \tag{22}$$

in which γ_C is typically assumed to be a constant of order unity [32]. However, in lifted flames, which are primarily controlled by chemical kinetics, regions of scalar mixing and reaction are spatially separated. In these systems, combustion is initiated in regions of low mixing intensities which favors autoignition. With increasing downstream distance, passive scalar mixing decreases and chemical reactions approach equilibrium conditions. Therefore, the assumption of constant γ_C is most likely only a zeroth-order approximation, and may not be adequate for lifted flames. This was demonstrated in Ref. [33] where an extended ignition region was obtained that could be attributed to an under-prediction of the reactive scalar mixing frequency. To accommodate for variations in the time scale ratio, it is proposed to model γ_C as

$$\gamma_C = \Gamma(1 - C/C^{\infty}), \tag{23}$$

where C^{∞} denotes the steady-state composition, and Γ is a constant that is set to 3.0. Through this model, the mixing frequency $1/\tau_C$ increases as the flame approaches steady-state, and leads to decaying subgrid scalar fluctuations of the progress variable. The proposed model and the model sensitivities will be tested, and results will be compared with experimental data in Section 5.

In this context it is noted that other closure formulations have been proposed to model $\widetilde{\chi}_{C}^{\mathrm{res}}$ [9,32], and their performance will be compared in future work.

3. Experimental configuration and computational setup

The experiment used for validating the UFPV combustion model corresponds to the vitiated co-flow burner, which was experimentally studied by Cabra et al. [6]. The experimental setup consists of a central fuel pipe with a diameter of $D_{\mathrm{ref}} = 4.57$ mm, through which a methane/air mixture at a temperature of 314 K is supplied. The jet exit velocity is $U_{\mathrm{ref}} = 100$ m/s. The Reynolds number based on the fuel nozzle diameter, exit velocity, and kinematic viscosity of the fuel mixture is 24,200, and the value of the stoichiometric

Table 1
Reference parameters for the lifted jet flame simulation.

Parameter	Units	Jet	Co-flow
d	m	4.57×10^{-3}(=D_{ref})	0.210
U	m/s	100(=U_{ref})	5.4
T	K	314	1355
X_{O_2}	–	0.1452	0.1193
X_{N_2}	–	0.5243	0.7285
X_{H_2O}	–	0.0029	0.1516
X_{CH_4}	–	0.3275	0.0003
X_{H_2}	–	0.0001	0.0001
X_{OH}	–	–	0.0002
Z_{st}	–	0.177	

mixture fraction is $Z_{st} = 0.177$. The co-flow consists of reaction products from a premixed hydrogen/air combustion. It is reported that the product mixture, consisting of oxygen, nitrogen, and water, is uniform across the co-flow stream, and the temperature is 1355 K. The co-flow has a diameter of 210 mm and is surrounded by an exit collar to prevent entrainment of ambient air into the flame. The experimental parameters are summarized in Table 1.

The Favre-filtered governing equations are solved in a cylindrical coordinate system [14]. The geometry is non-dimensionalized by the jet nozzle diameter D_{ref} and the computational domain is $90D_{ref} \times 30D_{ref} \times 2\pi$ in axial, radial, and circumferential directions, respectively. The axial direction is discretized with 256 grid points following a linear growth rate, and 150 grid points are used in radial direction. The circumferential direction is equally spaced and uses 64 points, resulting in a total number of approximately 2.5 million grid points. The minimum and maximum filter widths are $\Delta_{min} = 4 \times 10^{-2} D_{ref}$ (at the centerline near the nozzle exit) and $\Delta_{max} = 1.27 D_{ref}$ (outermost computational cell at the exit plane). For reference, the grid stretching diagram is shown in Fig. 4. The sensitivity of the LES results to the grid resolution has been investigated by refining the grid in the nozzle near-region using a total of 3.7 million grid points. In this grid-refinement study the UFPV model was used. From this study is was found that the shear layer, mixture fraction field, and flamebase are only weakly affected by further grid refinement.

The turbulent inflow velocity profile was generated from a periodic pipe flow simulation. The chemistry is described by the GRI 2.11 mechanism [34], and the unsteady flamelet calculations have been performed using the FLAMEMASTER code [35]. From the unsteady flamelets, the UFPV flamelet library is generated. To increase the table resolution, $\widetilde{Z''^2}$ was replaced by the mixedness, $\widetilde{S} = \widetilde{Z''^2}/(\widetilde{Z} - \widetilde{Z}^2)$, and the grid stretching in the directions of $\widetilde{Z}, \widetilde{S}$, and $\widetilde{C''^2}$ follow a geometric series. For the discretization of the chemistry table, 75 points are used for the $\widetilde{Z}$ and $\widetilde{C}$ directions, 20 points are used in the directions of $\widetilde{S}$ and $\widetilde{C''^2}$, and 20 points are used for $\widetilde{\chi}_{Z,st}$. For the generation of the flamelets and the chemistry table the inherent coarse grain parallelism of the problem has been exploited. To this end, unsteady flamelets evolving along individual trajectories are computed in parallel, and a parallel code is used to generate the chemistry table. With this, the generation of the UFPV chemistry table for the LES calculation could be performed in typically less than 12 h using 8 CPUs.

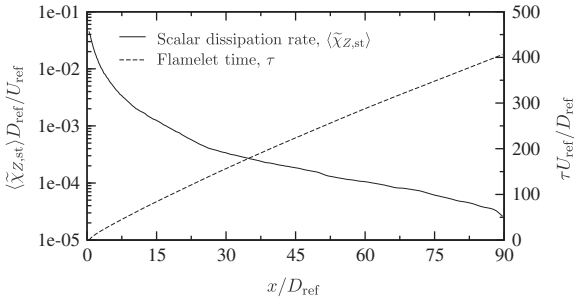

Fig. 5. Axial evolution of the stoichiometric scalar dissipation rate of mixture fraction and Lagrangian flamelet time, extracted from the LES results.

4. A priori study: significance of transient effects

In Section 1 it was pointed out that the accurate characterization of autoignition in turbulent flames requires the consideration of transient effects and turbulence/chemistry interaction. While effects due to coupling between turbulence and chemistry are quantified in the next section, the role of transient effects on the flame evolution are addressed in this *a priori* study.

The first part of this analysis consists in establishing a reference solution, which is here obtained from an unsteady Lagrangian flamelet calculation:

$$\text{Lagrangian flamelet model (LFM)}: \quad \partial_\tau C = \frac{1}{2}\chi_Z \partial_Z^2 C + \dot{\omega}_C. \tag{24}$$

To solve this equation, the scalar dissipation rate as a function of the flamelet time τ must be specified. This information is extracted from a LES calculation of the lifted flame configuration as described in Section 3. The Lagrangian flamelet time as a function of the axial distance x to the nozzle is computed as [36]

$$\tau(x) = \int_0^x [\langle\widetilde{u}_{st}\rangle(\xi)]^{-1}\, d\xi, \tag{25}$$

where $\widetilde{u}_{st} = \widetilde{u}|Z_{st}$ is the axial velocity which is conditioned on the stoichiometric mixture fraction. The angular brackets denote temporal and azimuthal averaging. The axial evolution of τ and $\langle\widetilde{\chi}_{Z,st}\rangle$ from the LES are illustrated in Fig. 5. From $\langle\widetilde{\chi}_{Z,st}\rangle$ the scalar dissipation rate profile is computed as

$$\chi_Z(\tau) = \langle\widetilde{\chi}_{Z,st}\rangle(\tau) F(Z), \tag{26}$$

with the definition of $F(Z)$ from Eq. (6).

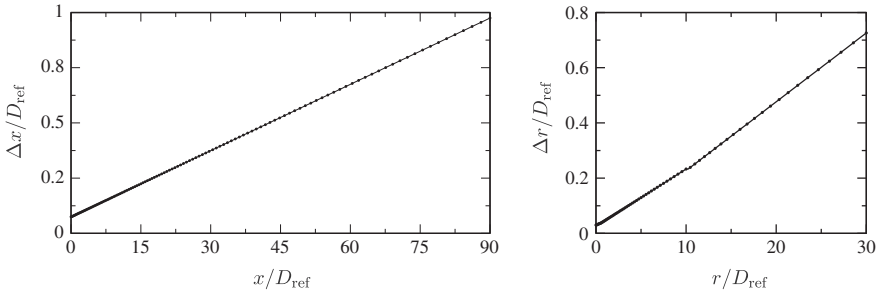

Fig. 4. LES grid stretching diagram: (left) axial direction; (right) radial direction. Only every second grid point is shown by the symbols.

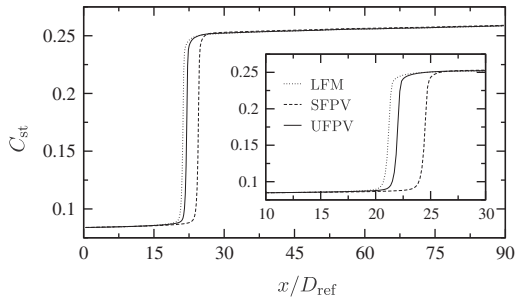

Fig. 6. Axial evolution of the reaction progress variable, evaluated at stoichiometric condition. The inset shows a zoom of the C_{st} profiles around the ignition region.

Table 2
Comparison of ignition location and ignition width obtained from the *a priori* study. The error is calculated with respect to the ignition location of the Lagrangian flamelet model.

	x_{ig}/D_{ref}	Error (%)	l_{ig}/D_{ref}
LFM	21.2	–	0.671
SFPV	24.5	15.6	0.697
UFPV	22.0	3.8	0.672

The flamelet solution to initialize Eq. (24) is obtained from a steady flamelet calculation with a scalar dissipation rate that is extracted from the LES results at an axial plane at the nozzle exit. The chemical source term $\dot{\omega}_C$, in Eq. (24) is a function of all species and temperature, and is directly evaluated from the flamelet equations. Since no further model assumptions in the source term calculation are invoked, the solution of this Lagrangian flamelet model is considered as the reference solution in this *a priori* study.

Next, the UFPV model, developed in Section 2.4, is cast into the form of Eq. (24). Since the turbulence/chemistry interaction is not considered in this *a priori* study the UFPV state relation in Eq. (19) reduces to:

$$\psi = \mathscr{G}^{U}_{\psi}(Z, C, \chi_{Z,st}). \tag{27}$$

This flamelet library is compiled from the solution of the unsteady flamelet equations as described in Section 2.4. With this, the Lagrangian form of the UFPV combustion model can be written as

$$\text{UFPV model}: \quad \partial_\tau C^U = \frac{1}{2}\chi_Z \partial_Z^2 C^U + \mathscr{G}^{U}_{\dot{\omega}_C}(Z, C^U, \langle\widetilde{\chi}_{Z,st}\rangle), \tag{28}$$

where $\langle\widetilde{\chi}_{Z,st}\rangle$ is evaluated from the LES data. Similarly, the Lagrangian form of the SFPV model can be written as

$$\text{SFPV model}: \quad \partial_\tau C^S = \frac{1}{2}\chi_Z \partial_Z^2 C^S + \mathscr{G}^{S}_{\dot{\omega}_C}(Z, C^S), \tag{29}$$

in which the chemical source term is obtained from the solution of the steady flamelet equations. It is emphasized that in the SFPV model a time-dependent transport equation for the reaction progress variable is solved, in which the chemical source term is computed from the steady flamelet equations. This is the main modeling assumption in the SFPV-formulation.

Eqs. (24), (28), and (29) are solved subject to the same initial conditions, prescribed scalar dissipation rate profiles, and precompiled state relations $\mathscr{G}^{S}_{\dot{\omega}_C}$ and $\mathscr{G}^{U}_{\dot{\omega}_C}$.

A comparison of the axial evolution of C_{st} obtained from both FPV models is shown in Fig. 6. In this figure the dotted line corresponds to the solution of the Lagrangian flamelet model, and the dashed and solid lines denote the SFPV and UFPV results, respectively.

The Lagrangian flamelet model predicts the ignition location at $x_{ig} = 21.2D_{ref}$ and an ignition width of $l_{ig} = 0.671D_{ref}$ (see Table 2). Here, the ignition width is defined as

$$l_{ig} = [\max(\partial_x C_{st})]^{-1}\Delta C_{st}. \tag{30}$$

Compared to the LFM results, the SFPV model predicts the ignition location at $x_{ig} = 24.5D_{ref}$, which corresponds to a 15% over-prediction. The reason for this discrepancy can be explained by expanding Eq. (29) as

$$\partial_\tau C^S = \frac{1}{2}(\chi_Z - \widehat{\chi}_Z)\partial_Z^2 C^S + \underbrace{\frac{1}{2}\widehat{\chi}_Z \partial_Z^2 C^S + \mathscr{G}^{S}_{\dot{\omega}_C}(Z, C^S)}_{=0 \text{ (Steady flamelet solution)}}, \tag{31}$$

where $\widehat{\chi}_Z$ denotes the scalar dissipation rate at the S-shaped curve. This shows that in the SFPV model the temporal derivative is related to the difference in scalar dissipation rates between the states described by the SFPV and steady flamelet solutions.

Compared to the SFPV results, the UFPV model significantly improves the prediction of the ignition location, deviating by less than 4% from that of the LFM results. This in turn confirms that the UFPV model accurately captures the transient ignition process in the absence of turbulence/chemistry interaction. An analysis that is not presented here, showed that the minor discrepancies between LFM and UFPV predictions are attributed to differences in the flamelet evolution. The difference in the UFPV model results from the construction of the UFPV flamelet library, and quantifies the significance of flame history effects that were discussed in Section 2.4.

5. LES results

In this section, results from LES calculations of the lifted flame configuration are discussed. Three LES computations are performed: In the first LES calculation, the UFPV model, developed in Sections 2.4 and 2.5, is used. The second LES calculation employs the SFPV model, and is used to quantify transient flame effects *a posteriori*. To investigate the interaction between turbulence and chemistry, the last calculation employs the UFPV model in which subgrid fluctuations of the progress variable are not considered. For this, a Dirac delta function is used instead of the SMLD to model $P(\Lambda)$ in Eq. (15). Additional calculations are performed in order to assess the model sensitivity with respect to model parameters and co-flow temperature.

Statistical results, denoted by angular brackets, are obtained from azimuthal and temporal averaging of the instantaneous flow field quantities, and Favre-averaged quantities are computed as $\{\widetilde{\psi}\} = \langle\overline{\rho}\widetilde{\psi}\rangle/\langle\overline{\rho}\rangle$.

5.1. Instantaneous and mean flow field structure

Instantaneous and averaged temperature fields obtained from all three simulations are illustrated in Fig. 7. The solid line in these figures corresponds to the isocontour of the stoichiometric mixture fraction. From the instantaneous temperature field obtained from the UFPV simulation (Fig. 7a), it can be seen that up to approximately $40D_{ref}$ downstream of the jet nozzle fuel and oxidizer mix without significant heat release. Following this approximately inert mixing zone, a transition region between $40 \leqslant x/D_{ref} \leqslant 60$ is apparent, in which the temperature increases due to autoignition. Beyond a distance of 60 nozzle diameters above the jet exit the flame is continuously burning, and some entrainment of fluid from the co-flow into the flame core can be observed.

The LES prediction from the SFPV model (Fig. 7b) shows a significantly different flame behavior. After a considerable reduction of the inert mixing region, the flame rapidly ignites at $22D_{ref}$, and a

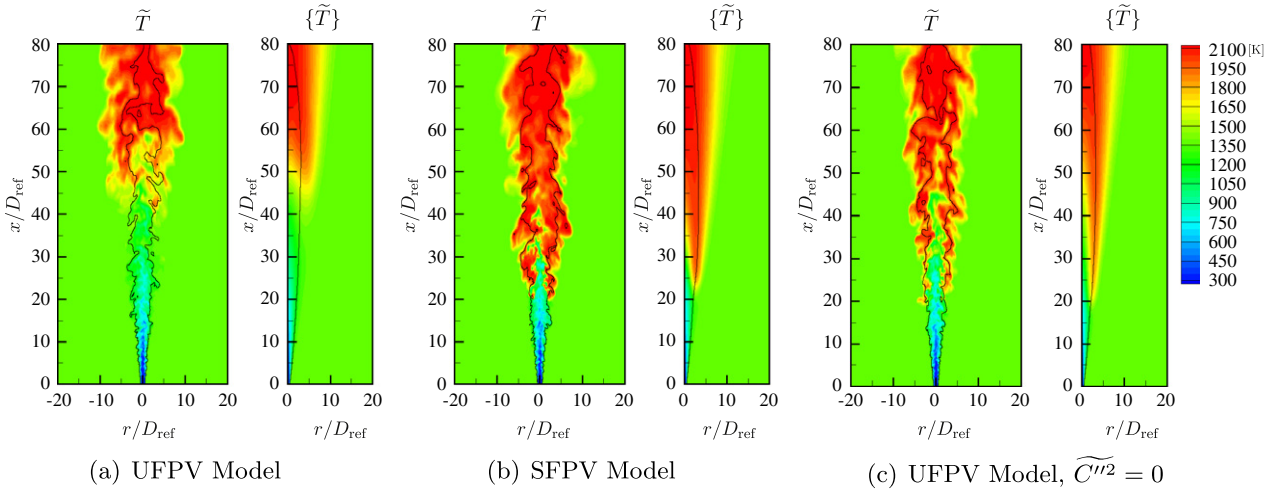

Fig. 7. Instantaneous and averaged temperature fields obtained from (a) UFPV model, (b) SFPV model, and (c) UFPV model with $\widetilde{C''^2} = 0$. The solid line shows the location of the stoichiometric mixture fraction, $\widetilde{Z}_{\rm st} = 0.177$.

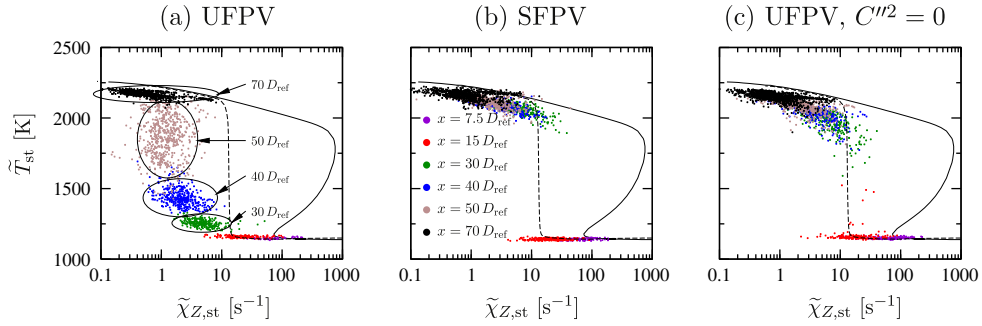

Fig. 8. Scatter plots of Favre-filtered temperature as a function of stoichiometric scalar dissipation rate obtained from (a) UFPV model, (b) SFPV model, and (c) UFPV model with $\widetilde{C''^2} = 0$. For reference, the S-shaped curve is shown by the solid line, and the dashed line illustrates the LFM ignition trajectory from the *a priori* study.

transition region, as observed in the UFPV simulation, is non-existing.

Flow field results from the UFPV model without consideration of subgrid progress variable fluctuations are shown in Fig. 7c. Compared to the other simulation results the following two observations can be made: First, the predicted lift-off height is three nozzle diameters shorter than that predicted by the SFPV model. Interestingly, this result is in qualitative agreement with observations from the *a priori* study (see Fig. 6 and Table 2). The second observation is related to differences in the flame structure prediction between different models. The instantaneous and mean temperature results in Fig. 7c show that the UFPV model with $\widetilde{C''^2} = 0$ yields a smaller spreading rate of the flame in radial direction compared to the SFPV results. This, in turn, is an indication of the ignition process, which is confined to a narrow region on the lean part of the flame, and was discussed in Section 2.4 in the context of Fig. 2b.

The instantaneous temperature field in Fig. 7c shows that the UFPV model with $\widetilde{C''^2} = 0$ results in a faster flame ignition. Neglecting the subgrid scale contribution of the progress variable assumes that a computational cell is occupied by a single flame state that is determined from the UFPV state relation. Since autoignition is confined to localized regions that are computationally not fully resolved, setting $\widetilde{C''^2} = 0$ extends the autoignition over the entire computational cell, which results in an over-prediction of flame ignition.

Single point data at six different axial locations in the jet flame are sampled from all three simulations. These data are presented in the form of scatter plots in Fig. 8. For reference, the steady flamelet solution of the S-shaped curve is shown by the solid line, and the dashed line illustrates the LFM ignition trajectory from the *a priori* study. The instantaneous scatter plots obtained from the UFPV simulation (Fig. 8a) show that the ignition process extends between 30 and 50 nozzle diameters. During the ignition process fluctuations in scalar dissipation rate are significant, which is apparent from the broad scattering in the $\widetilde{\chi}_{Z,\rm st}$-direction. A comparison with the UFPV modeling results, in which subgrid fluctuations in C are not considered (Fig. 8c), illustrates the effect of turbulence/chemistry interaction on the flame evolution. This coupling results in a shift in the ignition process towards smaller values of the scalar dissipation rate.

Scatter data from the SFPV calculation (Fig. 8b) closely resemble the LFM ignition trajectory (shown by the dashed line). However, contrary to the UFPV results, these scatter data follow a distribution that is primarily confined to the upper stable branch and the extended mixing line of the S-shaped curve.

5.2. Statistical flow field results

A comparison of Favre-averaged results for mixture fraction and temperature along the jet centerline are presented in Fig. 9. Mean mixture fraction profiles from the UFPV model can be considered to be in excellent agreement with experimental results. The other

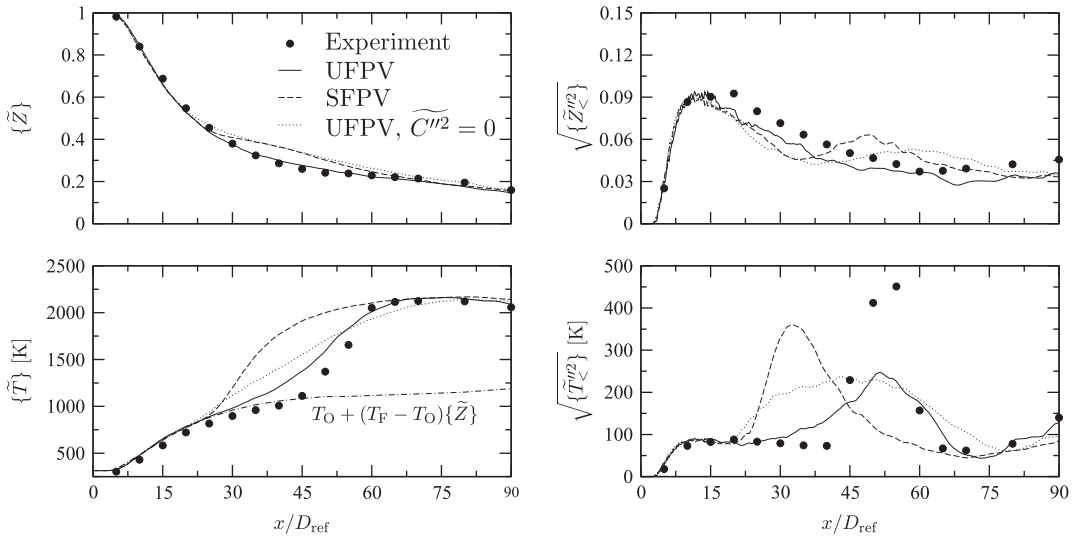

Fig. 9. Comparison of measured (symbols) and calculated (lines) mean and rms statistics of mixture fraction and temperature along the centerline of the Cabra-flame.

two models considerably over-predict $\{\widetilde{Z}\}$ in the region $30 \leqslant x/D_{ref} \leqslant 60$. Note that outside of this region, where transient effects are not significant, all simulations yield identical results, which demonstrates the consistency of all models.

Predictions for mean and rms temperature profiles are compared with experimental data in the bottom row of Fig. 9. For reference, the dash-dotted line shows the temperature increase due to scalar mixing between reactants, which is approximated as:

$$\{\widetilde{T}\}_{mix} = T_O + (T_F - T_O)\{\widetilde{Z}\}, \tag{32}$$

where T_F and T_O denote the temperature in the fuel and oxidizer stream, respectively. This curve shows that up to a distance of $45D_{ref}$ the increase in centerline temperature is primarily controlled by the scalar mixing process, and that heat release effects become significant for $x > 45D_{ref}$. The UFPV model accurately captures the experimentally reported mean temperature evolution. Small discrepancies, that arise from an advanced ignition location and a slightly lower temperature rise over the course of the autoignition process are evident. The end of the ignition location is accurately captured with the UFPV model.

The SFPV model predicts a significantly faster ignition process, which results in the flame reaching a steady-state condition at a distance of $45D_{ref}$ from the nozzle exit. This will further be discussed in the analysis of mixture fraction-conditional results in Fig. 10.

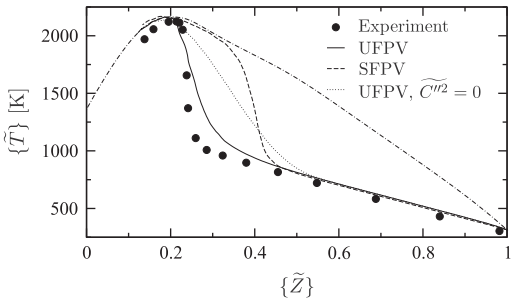

Fig. 10. Comparison of the predicted mean temperature as a function of $\{\widetilde{Z}\}$ along the centerline with experimental data. The dash-dotted curve corresponds to the steady-state flamelet solution evaluated for $\chi_{Z,st} = 1.0\ s^{-1}$.

Simulation results from the UFPV model without consideration of progress variable fluctuations are represented by the dotted line. It is interesting to point out that this model predicts a considerably larger ignition region over which the flame temperature increases only slowly.

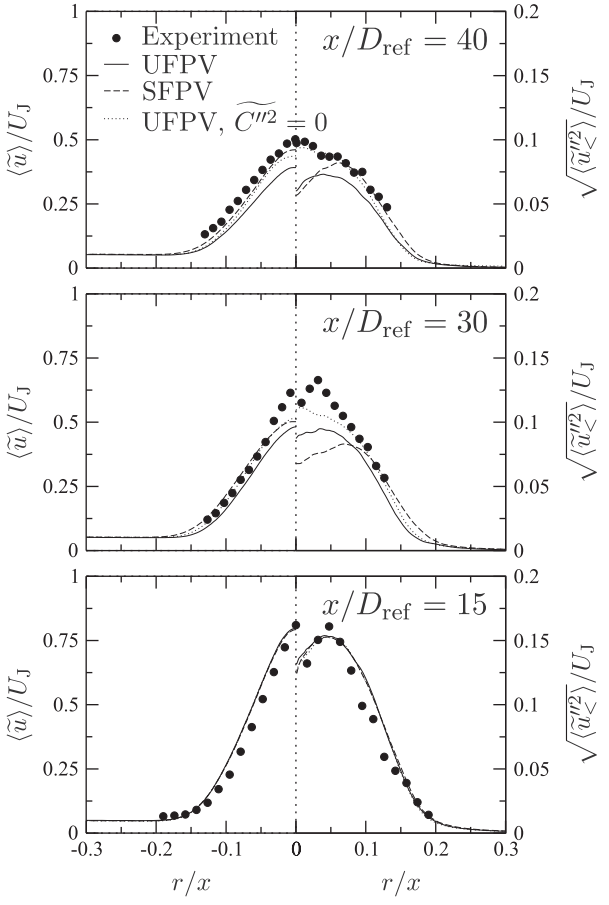

Fig. 11. Comparison of mean and rms axial velocity. The measurements are from Ref. [37], corresponding to an experimental configuration with a co-flow temperature of 1380 K.

Results for rms temperature fluctuations are shown in the bottom right of Fig. 9. While the UFPV model accurately captures the location of the peak temperature fluctuations, the peak value is under-predicted by approximately 200 K. The SFPV model predicts a considerably earlier peak location, and the UFPV model with $\widetilde{C''^2} = 0$ shows an extended region over which temperature fluctuations are appreciable.

The mean temperature as a function of mean mixture fraction along the jet centerline is illustrated in Fig. 10. Although the UFPV model under-predicts the rapid increase in temperature around $\{\widetilde{Z}\} = 0.25$, the model shows significant improvements over the SFPV model. It can be seen that the solution from the SFPV model approaches the steady-state solution at $\{\widetilde{Z}\} = 0.35$, which corresponds to a physical location of $35D_{\mathrm{ref}}$ above the jet nozzle exit.

Radial profiles for the mean and rms axial velocity component at x/D = 15, 30, and 40 are shown in Fig. 11. For reference, measurements for a co-flow temperature of 1380 K are shown by the symbols. These measurements are taken by Gordon [37]. The mean velocity profiles are in reasonable agreement with the experimental results. Although deviations between the three simulations are apparent near the centerline, the predicted velocity field in the region around the flamebase ($r/x \approx 0.14$) are within experimental uncertainties. This suggests that the predicted velocity fields are not responsible for the differences in lift-off height and flamebase stabilization.

Radial profiles for mean quantities of mixture fraction, temperature, and species mass fractions of H_2O,CO_2, and CO are compared with experimental data in Fig. 12. Favre-averaged mixture fraction profiles are shown in the first row. Results obtained from the UFPV model are in good agreement with experimental data for measurement stations $x \geqslant 30D_{\mathrm{ref}}$. Although the other two models correctly capture the axial spreading, the mixture fraction profiles are over-predicted for x/D_{ref} = 30, 40, and 50. This over-prediction is primarily confined to the fuel-rich side of the flame. Predictions for radial temperature profiles from the UFPV model are in reasonable agreement with measurements, and the location of the peak temperature and flame width are adequately captured by the UFPV model. Similarly, predictions for major species of H_2O and CO_2 are in good agreement with experiments. Results for CO are shown in the bottom row of Fig. 12. In the transition region between 30 and 50 nozzle diameters, the SFPV model and the UFPV formulation without turbulence/chemistry interaction over-predict the CO-formation by a factor of two, which explains the apparent over-prediction of the CO_2 profiles for both simulations.

From the analysis of radial profiles, it can be seen that all three models yield different results in the region where transient effects and turbulence/chemistry interaction are of particular significance. Since the UFPV model captures the main flame dynamics in this transition region, this suggests that the UFPV model contains the fundamental thermochemical mechanisms for describing flame autoignition. In this respect it is also encouraging that all three models provide very similar results in regions in which transient effects are not of relevance (*i.e.*, $x/D_{\mathrm{ref}} \leqslant 25$ and $x/D_{\mathrm{ref}} \geqslant 65$), which is an indication of the consistency of all models.

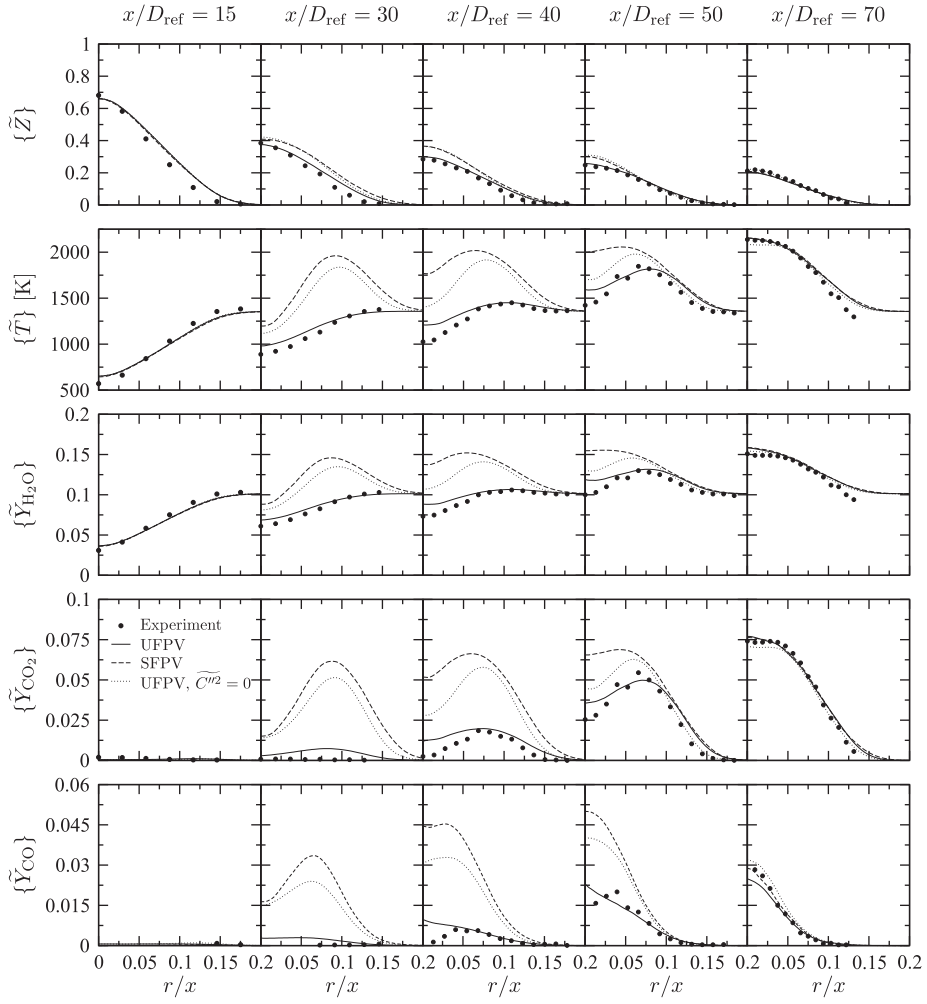

Fig. 12. Comparison of radial profiles between simulations and experiments, for mixture fraction, temperature, and species mass fractions of H_2O, CO_2, and CO.

The lift-off height was determined from the location of the maximum gradient of the mean OH mass fraction, as described by Gordon *et al.* [7]. The UFPV calculation predicts a lift-off height of $45D_{\mathrm{ref}}$. This result is within 10% of the experimental results reported in Ref. [7], using the same diagnostics. Experimental investigations showed that the flame lift-off height is strongly dependent on the temperature in the co-flow stream. From the experimental data of Cabra et al. [6], the sensitivity of the lift-off height, l_{Exp}, with respect to the co-flow temperature, T_{co}, is determined from a least-square analysis as $\partial l_{\mathrm{Exp}}/\partial T_{\mathrm{co}} \simeq -0.3 D_{\mathrm{ref}}/\mathrm{K}$ for $1350\ \mathrm{K} \leqslant T_{\mathrm{co}} \leqslant 1430\ \mathrm{K}$. Additional calculations for a co-flow temperature of 1430 K were performed using the UFPV model. From these results the model sensitivity was evaluated as $\partial l_{\mathrm{UFPV}}/\partial T_{\mathrm{co}} \simeq -0.072\ D_{\mathrm{ref}}/\mathrm{K}$. In order to further analyze the model performance, a parametric study of the UFPV model was conducted, in which the model coefficient Γ in Eq. (23) was varied over the range $2 \leqslant \Gamma \leqslant 4$. From these calculations the sensitivity coefficient $\partial\ l_{\mathrm{UFPV}}/\partial\Gamma \simeq 4D_{\mathrm{ref}}$ was determined, which showed that the lift-off height is weakly dependent on this parameter, and this sensitivity is independent of the co-flow temperature.

5.3. Conditional flow field results

Mixture fraction-conditional results for temperature and species mass fractions of H_2O, CO_2, CO, and OH are presented in Fig. 13. The comparison of temperature profiles shows that the UFPV model captures the autoignition process. While slight overpredictions of temperature around the stoichiometric condition are evident at the first two measurement locations, predictions at further downstream locations are in very good agreement with experimental results; UFPV simulation results for H_2O and CO_2 are in equally good agreement. Compared to these results the SFPV model predicts a fully burning flame state already at $x = 30D_{\mathrm{ref}}$. It is interesting to point out that the SFPV model also predicts significant heat release and combustion in the rich part of the flame, which is not observed from the experimental data. The onset of this partially premixed burning occurs at $x = 40D_{\mathrm{ref}}$ and is particularly evident for temperature and species profiles of H_2O and CO_2. Results for CO mass fraction, predicted by the UFPV model, are in good agreement with the measurements.

Conditional data for the hydroxyl radical, presented in the last row of Fig. 13, show that the UFPV model adequately captures the peak location and formation process of OH throughout the flame; however, a shift in the predicted location of the peak OH mass fraction towards richer mixture composition is apparent. In contrast, the other two models are not able to capture the sensitivity of the OH formation, and predict OH profiles with nearly constant shape and peak location for all measurement stations.

Overall, conditional results for temperature and species mass fractions predicted with the UFPV model are in good agreement with experimental data, and the model adequately captures the transient flame ignition process.

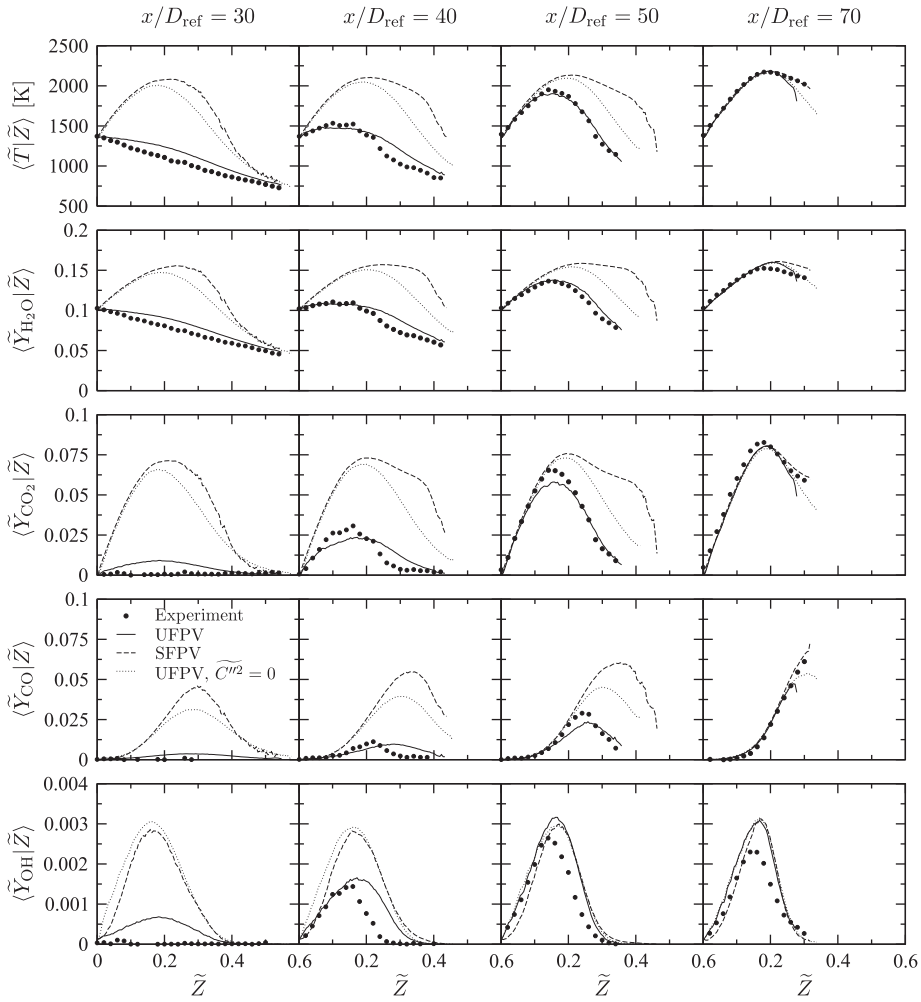

Fig. 13. Comparison of measured (symbols) and calculated (lines) conditional mean temperature and mean mass fractions of H_2O, CO_2, CO, and OH at four axial locations in the flame.

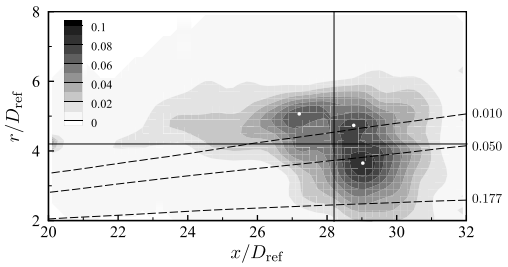

Fig. 14. PDF of the flame stabilization point. The dashed lines correspond to isocontours of the mean mixture fraction with $\{\widetilde{Z}\} = \{0.01, 0.05, 0.177\}$ (from top to bottom), and the solid lines denote the mean axial and radial locations of the stabilization point.

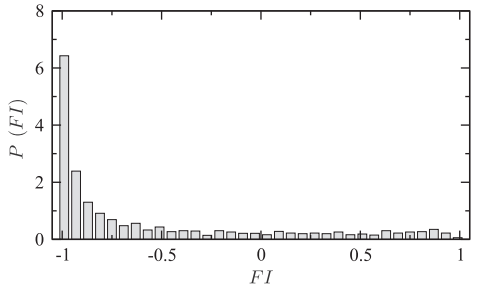

Fig. 15. PDF of the flame index *FI*, evaluated at the flame stabilization point.

5.4. Flamebase analysis

In this section, the structure and the stabilization mechanism at the flamebase are analyzed. To identify the autoignition events at the flamebase, associated with the formation of OH through the consumption of intermediate HO_2 species, an isocontour of the OH mass fraction with $\widetilde{Y}_{\mathrm{OH}} = 10^{-3}$ has been selected. This criterion is identical to that used in Ref. [2], and our analysis showed that this marker is adequate in identifying the onset of ignition at the flamebase. With this, the flamebase is identified as the most upstream location of this isocontour, and the simulation results are sampled to extract this stabilization point. The PDF for the stabilization location is shown in Fig. 14. The dashed lines correspond to three isocontours of the mean mixture fraction with $\{\widetilde{Z}\} = \{0.01, 0.05, 0.177\}$, and the solid lines denote the mean axial and radial locations of the stabilization point. From this statistical analysis it can been seen that the stabilization point, defined by the criterion above, is confined to the fuel lean region. While the flamebase fluctuations are confined to a relatively narrow region in radial direction, considerable variations in axial direction are apparent. In addition, statistical results of Fig. 14 suggest that the flame stabilizes at three preferred locations, that are indicated by the white symbols. An analysis of the flow field structure showed that the scalar dissipation rate at the stabilization point is below the critical value at ignition, which is consistent with the scatter plot shown in Fig. 8.

To characterize the combustion mode at the stabilization location, the flame index [38] is evaluated. The flame index *FI*, quantifies the alignment between the fuel and oxidizer gradients, and is here defined as

$$FI = \frac{\nabla\widetilde{Y}_{\mathrm{CH_4}} \cdot \left(\nabla\widetilde{Y}_{\mathrm{O_2}} - Y^{\mathrm{F}}_{\mathrm{O_2}}\nabla\widetilde{Z}\right)}{|\nabla\widetilde{Y}_{\mathrm{CH_4}}|\left|\left(\nabla\widetilde{Y}_{\mathrm{O_2}} - Y^{\mathrm{F}}_{\mathrm{O_2}}\nabla\widetilde{Z}\right)\right|}, \tag{33}$$

in which $\widetilde{Y}_{\mathrm{CH_4}}$ and $\widetilde{Y}_{\mathrm{O_2}}$ are obtained from the UFPV chemistry table, and the term $Y^{\mathrm{F}}_{\mathrm{O_2}}\nabla\widetilde{Z}$ is subtracted to account for the oxygen in the fuel stream. A value of $FI = -1$ defines a diffusion mode and $FI = 1$ corresponds to the premixed autoignition regime.

The PDF of the flame index, evaluated at the stabilization point, is shown in Fig. 15. These statistical results show that ignition occurs primarily in the diffusion mode, and a quantitative analysis showed that 50% of all ignition events occur under conditions in which the alignment angle between fuel and oxidizer gradients exceeds $3/4\pi$. The result that the stabilization location is primarily controlled by non-premixed conditions is in agreement with previous DNS-studies [2,39].

6. Conclusions

An unsteady flamelet/progress variable model has been developed for the prediction of autoignition in turbulent lifted flames. The model is a consistent extension to the steady flamelet/progress variable approach, and employs an unsteady flamelet formulation to describe the transient evolution of all thermochemical quantities during the flame ignition process. In this UFPV model, all thermochemical quantities are parameterized by mixture fraction, reaction progress parameter, and stoichiometric scalar dissipation rate. The particular advantage of the UFPV model over previously developed unsteady flamelet formulations is that in this model the flamelet time is replaced by physical quantities, which leads to significant simplifications in computation and parameterization of the thermodynamic state space. The UFPV model was analyzed in an *a priori* study to assess underlying modeling assumptions that arise from the population of the state space.

A presumed PDF closure model is employed to evaluate Favre-averaged thermochemical quantities. For this a beta-distribution is used for the mixture fraction, a statistically most-likely distribution is employed for the reaction progress parameter, and the distribution of the stoichiometric scalar dissipation rate is modeled by a Dirac delta function.

The UFPV model was applied in LES of a lifted flame in a vitiated co-flow, and simulation results are compared with experimental data. Additional calculations with the SFPV model and a modified UFPV formulation are carried out to investigate transient effects and to quantify the significance of turbulence/chemistry interaction *a posteriori*. Simulation results show that the UFPV model leads to significantly improved predictions of flame structure, lift-off height, and spatiotemporal evolution of the flow field. Although the UFPV model predicts a slightly faster ignition behavior, statistical results for mixture fraction, temperature, and species are in good agreement with experimental data. In contrast, the SFPV model results in a significantly faster ignition process that is not in agreement with the experimental results. Furthermore, the importance of turbulence/chemistry interaction was analyzed, and it was shown that by neglecting subgrid fluctuations of the progress variable the UFPV model predicts an extended ignition region.

Mixture fraction-conditional data for temperature and species mass fractions of H_2O,CO_2,CO, and OH are analyzed and compared with experimental results. In addition, scatter plots show that the UFPV model occupies a large portion of the unsteady flamelet space, while the scatter data for the SFPV model give a much faster ignition process, which is consistent with the findings from the *a priori* study. The SFPV results also show that the predicted flame states are primarily confined to the upper stable branch of the S-shaped curve, which explains the short ignition time and reduction in the lift-off height.

For future work it would be interesting to also account for scalar dissipation fluctuations in the presumed PDF closure. It is anticipated that the statistical consideration of these subgrid scale fluctuations would further improve the simulation results of the UFPV model.

Acknowledgment

The authors gratefully acknowledge financial support through the Office of Naval Research under Contract No. N00014-10-1-0561 with Dr. H. Scott Coombe as technical monitor.

References

[1] A.H. Lefebvre, Gas Turbine Combustion, Taylor & Francis, New York, 1999.
[2] C.S. Yoo, R. Sankaran, J.H. Chen, J. Fluid Mech. 640 (2009) 453–481.
[3] H. Pitsch, Ann. Rev. Fluid Mech. 38 (2006) 453–482.
[4] H. Pitsch, M. Ihme, An unsteady/flamelet progress variable method for LES of nonpremixed turbulent combustion, AIAA Paper 2005-557, 2005.
[5] H. Pitsch, H. Steiner, Phys. Fluids 12 (10) (2000) 2541–2554.
[6] R. Cabra, J.-Y. Chen, R.W. Dibble, A.N. Karpetis, R.S. Barlow, Combust. Flame 143 (2005) 491–506. <http://www.me.berkeley.edu/cal/vcb/data/VCMAData.html>.
[7] R.L. Gordon, A.R. Masri, S.B. Pope, G.M. Goldin, Combust. Flame 151 (2007) 495–511.
[8] K. Gkagkas, R.P. Lindstedt, Proc. Combust. Inst. 31 (2007) 1559–1566.
[9] P. Domingo, L. Vervisch, D. Veynante, Combust. Flame 152 (2008) 415–432.
[10] J.-B. Michel, O. Colin, C. Angelberger, D. Veynante, Combust. Flame 156 (2009) 1318–1331.
[11] M. Germano, U. Piomelli, P. Moin, W.H. Cabot, Phys. Fluids A 3 (7) (1991) 1760–1765.
[12] D.K. Lilly, Phys. Fluids A 4 (3) (1992) 633–635.
[13] S. Ghosal, J. Comput. Phys. 125 (1) (1996) 187–206.
[14] C.D. Pierce, P. Moin, J. Fluid Mech. 504 (2004) 73–97.
[15] M. Ihme, C.M. Cha, H. Pitsch, Proc. Combust. Inst. 30 (2005) 793–800.
[16] N. Peters, Prog. Energy Combust. Sci. 10 (3) (1984) 319–339.
[17] N. Peters, Combust. Sci. Technol. 30 (1983) 1–17.
[18] N. Peters, Turbulent Combustion, Cambridge University Press, Cambridge, 2000.
[19] M. Ihme, H. Pitsch, Phys. Fluids 20 (2008) 055110.
[20] A. Liñán, A. Crespo, Combust. Sci. Technol. 14 (1–3) (1976) 95–117.
[21] C. Wall, B.J. Boersma, P. Moin, Phys. Fluids 12 (10) (2000) 2522–2529.
[22] J. Jiménez, A. Liñán, M.M. Rogers, F.J. Higuera, J. Fluid Mech. 349 (1997) 149–171.
[23] E.T. Jaynes, Phys. Rev. 106 (4) (1957) 620–630.
[24] C.H. Shannon, Bell System Technol. J. 27 (3) (1948) 379–423.
[25] I.J. Good, Ann. Math. Stat. 34 (3) (1963) 911–934.
[26] S.B. Pope, J. Non-Equilib. Thermodyn. 4 (1979) 309–320.
[27] C.-S. Fang, J.R. Rajasekera, H.-S.J. Tsao, Entropy Optimization and Mathematical Programming, Kluwer Academic Publisher, Boston, 1997.
[28] M. Ihme, H. Pitsch, Combust. Flame 155 (2008) 90–107.
[29] T. Poinsot, D. Veynante, Theoretical and Numerical Combustion, R.T. Edwards, Inc., Philadelphia, PA, 2001.
[30] R.O. Fox, Computational Models for Turbulent Reacting Flows, Cambridge University Press, Cambridge, 2003.
[31] M. Ihme, Pollutant formation and noise emission in turbulent non-premixed flames, PhD thesis, Stanford University, 2007.
[32] C.M. Cha, P. Trouillet, Phys. Fluids 15 (6) (2003) 1375–1380.
[33] M. Ihme, Y.C. See, Large-eddy simulation of a turbulent lifted flame in a vitiated co-flow, AIAA Paper 2009-239, 2009.
[34] C.T. Bowman, R.K. Hanson, D.F. Davidson, W.C. Gardiner, V. Lissianski, G.P. Smith, D.M. Golden, M. Frenklach, M. Goldenberg, GRI-Mech 2.11, 1997, <http://www.me.berkeley.edu/gri-mech/>.
[35] H. Pitsch, FLAMEMASTER V3.1: a C++ computer program for 0D combustion and 1D laminar flame calculations, 1998, <http://www.stanford.edu/group/pitsch/>.
[36] H. Pitsch, M. Chen, N. Peters, Proc. Combust. Inst. 27 (1998) 1057–1064.
[37] R.L. Gordon. A Numerical and Experimental Investigation of Autoignition. PhD thesis, University of Sydney, 2008.
[38] H. Yamashita, M. Shimada, T. Takeno, Proc. Combust. Inst. 26 (1996) 27–34.
[39] P. Domingo, L. Vervisch, J. Réveillon, Combust. Flame 140 (2005) 172–195.